Electronic Supplementary Material (ESI) for Journal of Materials Chemistry C.

Electronic Supplementary Information

Interrogating the CISS effect in chiral and paramagnetic organic radicals: the impact of the molecular spin over the total spin polarization

J. Alejandro De Sousa, Paula Mayorga-Burrezo, Sandra Míguez-Lago, José Catalán-Toledo, Raúl Ramos-Tomás, Ana Ortuño, Linda A. Zotti, Juan José Palacios, Araceli G. Campaña,* J. Veciana* and N. Crivillers*

Table of Contents

General methods

Cyclic voltammetry characterizations were performed with an AUTOLAB 204 equipped with NOVA 2.3 software. A Pt mesh was used as the counter electrode, Ag/AgCl 3 M KCl (E (Fc/Fc^+) *vs.* Ag/AgCl = 0.504V) was used as the reference electrode or Ag-wire as pseudo-reference electrode (using as internal reference Fc/Fc+ redox couple). For the electrochemical characterization of the SAMs, the modified substrate was used as the working electrode. All the experiments were done under an argon atmosphere.

EPR spectra were recorded at room temperature on a Bruker ESP 300 E spectrometer provided with a rectangular cavity T102 that works with an X band (9.5 GHz). The signal-to-noise ratio of spectra was increased by accumulation of scans using the F/F lock accessory to guarantee large field reproducibility. Precautions to avoid undesirable spectral distortion and line broadenings, such as those arising from microwave power saturation and magnetic field over modulation, were also considered to improve sensitivity.

UV-Vis absorption spectra in solution were acquired with a JASCO V-780 UV/Visible/NIR with quartz cuvettes (Hellma Analytics, QS material) with a 1 cm path length. A baseline correction was applied with the pure solvent spectrum.

ECD spectra in solution were acquired with a JASCO J-815 using quartz cuvettes (Hellma Analytics, QS material) with a 1 cm path length. ECD spectra of the films were acquired with an Olis DSM172 spectrophotometer equipped with a Hamamatsu 150 W xenon arc lamp or a fixed wavelength LED as light source, a Hamamatsu photomultiplier tube (PMT) as detector for absorbance and CD and a Hamamatsu photon counting detector for fluorescence and CPL measurements. Films were prepared on a square quartz coverslip, 19 x 19 x 0.5 mm thick (TED PELLA, INC. 26016), covered by Ti (2 nm)/Au (6 nm). A baseline correction was applied using the spectrum of the clean substrate (Quartz/$Ti_{(2\ nm)}$/$Au_{(6\ nm)}$).

HPLC analyses and enantiomeric resolution were carried out using an Agilent 1260 Infinity II chromatograph provided with quaternary pump VL (G7111A), automatic sample injector (G7129A), column thermostat (G7116A), DAD detector WR (G7115A) and an automatic sample collector (G1364F 1260 FC-AS). CHIRALPAK IG packed with amylose functionalized with tris(3-chloro-5 methylphenylcarbamate) immobilized on silica gel (5 mm) was used as analytical column. The column temperature was set at 5 ºC and the flow was constant during operation (1 mL/min).

The optical microscopy images were taken using an Olympus BX51 microscope equipped with a polarizer and analyzer. On the other hand, AFM images were acquired with a 5100 and 5500LS SPM system from Agilent Technologies. Data analysis was performed by using WSxM software.

Finally, X-ray diffraction measurements were carried out with a PANalytical X'Pert Pro MRD (Materials Research Diffractometer) diffractometer. The Cu K-alpha radiation 1.54187 Å was used.

1. Synthesis of PTM radical derivatives

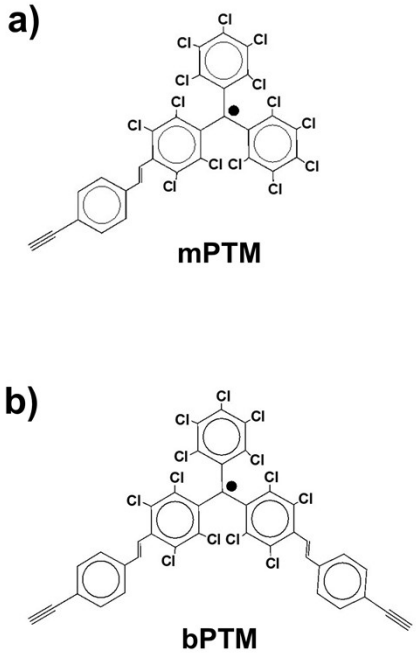

Scheme S1. Chemical structures for the mono- and bis-functionalized PTM derivatives, a) **mPTM** and b) **bPTM**

mPTM and **bPTM** (**Scheme S1**) were synthesized following the procedure developed previously in the group.[1] The radical character of the open-shell molecules was demonstrated by EPR and UV-Vis. **Figure S1a** shows the UV-Vis spectra of **mPTM** and **bPTM** in toluene, where a sharp peak around 385 nm is assigned to a SOMO→LUMO electronic transition, typically observed for this family of radicals (fingerprint of PTM radicals). The relative change of the peak intensity and the high absorption bands in the visible region for compound **bPTM** compared to **mPTM** is associated to the delocalization of the Highest Occupied Molecular Orbital (HOMO) on the substituents of the PTM core.[2]

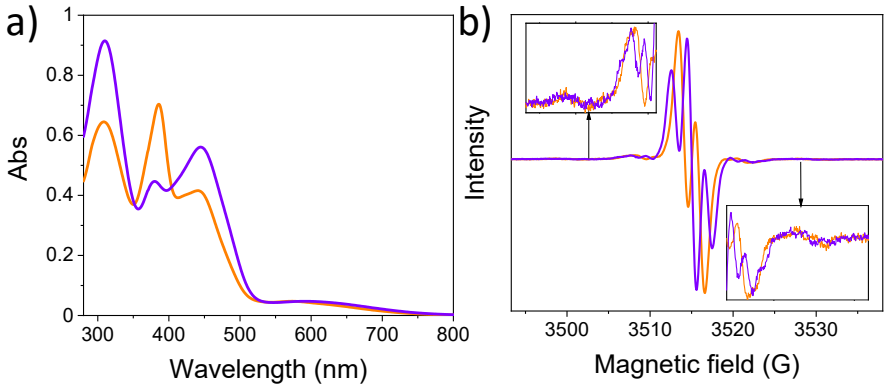

Figure S1. a) UV-Vis spectra of **mPTM** (orange) and **bPTM** (purple) in toluene (approximately 30 μM). b) EPR spectra of **mPTM** (orange) and **bPTM** (purple) in dichloromethane at room temperature. The insets show ^{13}C hyperfine coupling.

The EPR spectra (**Figure S1b**) show the central signal with a *g* value of 2.0020 typical for PTM radicals, near the free-electron *g* value of 2.0023, with two and three lines for **mPTM** and **bPTM**, respectively, and with a coupling constants of a(^{1}H) = 1.9 G (for **mPTM**) and 2.0 G (for **bPTM**), which are attributed to the hyperfine coupling with one or two vinylene protons (the H of the vinylene that is farther respect the central core of PTM rad). In addition, the weak satellites lines observed in the inset of **Figure S1b** are attributed to the coupling of the unpaired electron with the ^{13}C isotope of the α-carbon a($^{13}C_{\alpha}$) = 29.4 G (for **mPTM**) and 32.0 G (for **bPTM**), and aromatic carbons a($^{13}C_{ar}$)= 10-14 G (range for **mPTM** and **bPTM**). Since ^{13}C has a low natural abundance (1.1 %) the corresponding EPR signals are weak.

2. Enantiomeric resolution

Using a fraction collector coupled with the HPLC chromatograph, racemic solutions of compounds **mPTM** and **bPTM** (2 mg/mL) were separated in their corresponding enantiomeric forms, injecting 100 μL of the racemic solution into the column and, repeating the separation and collection operation several times. The conditions were: Eluent (v/v): 85:15 (**mPTM**) and 80:20 (**bPTM**) Hex:DCM under isocratic conditions; flow = 1 mL/min; T = 278 K; Detection at λ = 385.4 nm (**mPTM**) and 441.0 nm (**bPTM**). To avoid the racemization process, the collected fractions were maintained at -20 ºC, using an ice/NaCl bath. Futhermore, the solvent was removed in a rotary evaporator using an ice bath (0 ºC) and with very low pressure.

The enantiomeric excess was determined using the areas of the chromatographic peaks (**Figure S2**) using the following equations:

For M enantiomer:

$$[ee]_M = \left(\frac{A_M - A_P}{A_M + A_P}\right) x100\ \% \qquad \textbf{Equation S1}$$

For P enantiomer:

$$[ee]_P = \left(\frac{A_P - A_M}{A_M + A_P}\right) x100\ \% \qquad \textbf{Equation S2}$$

where A_M is the HPLC peak area of the Minus ***(M)***-enantiomer and A_P is the HPLC peak area of the Plus ***(P)***-enantiomer.

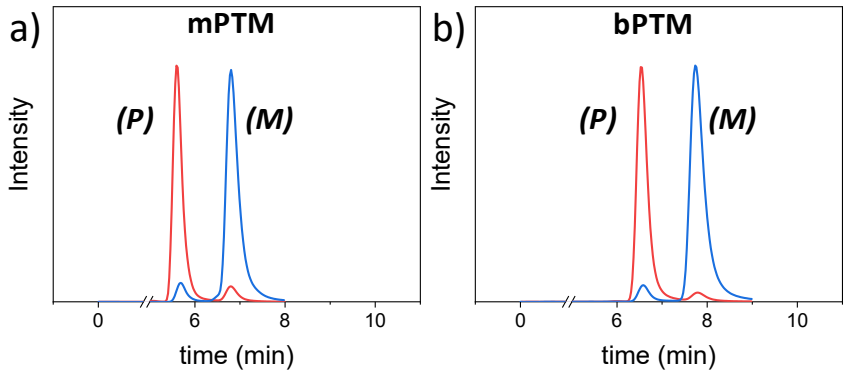

Figure S2. (CSP)-HPLC chromatograms of enantioenriched fractions for a) **mPTM** and b) **bPTM**, ***(P)*** (red) and ***(M)*** (blue) enantiomers.

3. DFT Calculations

The theoretical calculations (optimization, frequency and UV and ECD spectra) performed for both ***(M)*-mPTM** and ***(M)*-bPTM** were conducted using DFT at a UB3LYP/6-31G(d,p) level of calculation using PCM toluene solvent model. Given that B3LYP usually performs well for the transition energies, in both cases, the assignment was made according to the sign and relative intensities of transitions at ca. 520 nm and ca. 400 nm of opposite sign. In the specific case of ***(M)*-mPTM**, the mismatch between theoretical and experimental ECD spectra at wavelengths below 350 nm was attributed to the cancelation of transitions of similar intensity, very close in energy to each other. However, in the specific case of ***(M)*-bPTM**, the gaussian-composed envelope function from the aforementioned transitions (employing the same 0.333 eV for the UV-Vis peak half-width at half-height as for the **mPTM** derivative) shows a sign opposite to the experimentally observed below 350 nm.

Thus, in order to calculate the set of transitions in a more accurate way, a more extended basis set was employed (UB3LYP/6-311+G(d,p) with PCM toluene). In this case, the calculation resulted again in an inaccurate description of the ECD spectrum for the **bPTM** congener (**Figure S3.1**). The same problem was faced when the **mPTM** was computed (**Figure S3.2**).

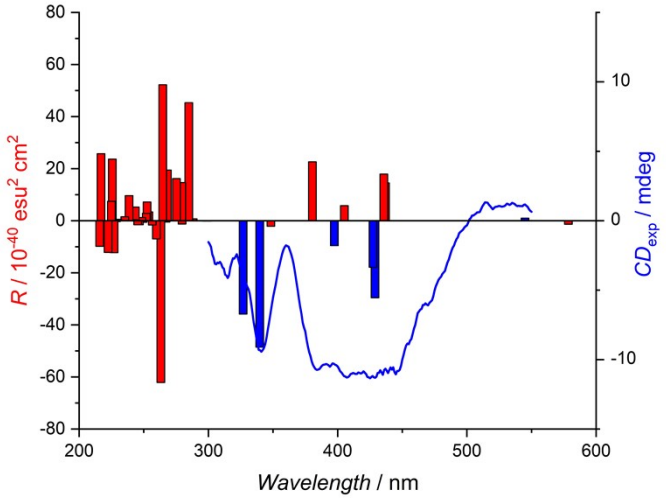

Figure S3.1 Experimental ECD spectrum of **(*P*)-bPTM** in toluene (blue line). Theoretical ECD spectrum of **(*P*)-bPTM** at the B3LYP/6-311+G(d,p) level of calculation (red columns). Blue R columns mark coincident theoretical-experimental matching. Theoretical spectra were corrected with an 80 nm blueshift.

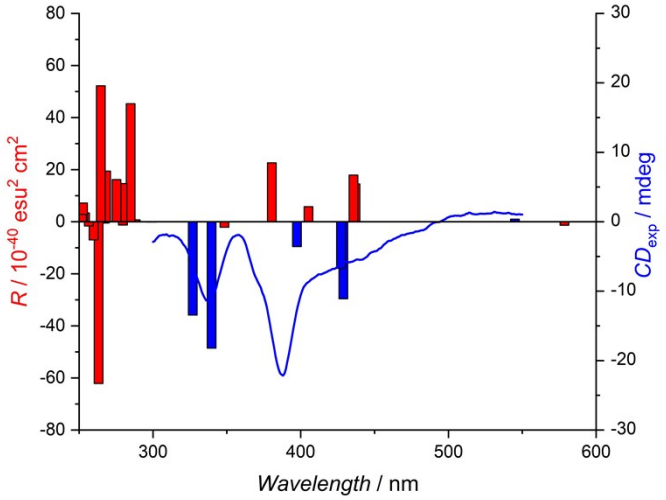

Figure S3.2. Experimental ECD spectrum of **(*P*)-mPTM** in toluene (blue line). Theoretical ECD spectrum of **(*P*)-mPTM** at the B3LYP/6-311+G(d,p) level of calculation (red columns). Blue R columns mark coincident theoretical-experimental matching. Theoretical spectra were corrected with an 80 nm blueshift.

Another attempt to better reproduce the theoretical-experimental ECD match was based on increasing the number of calculated transitions from 50 to 100, reaching this way transitions below 250

nm. Thus, starting from the geometries calculated at the B3LYP/6-31G(d,p) with PCM toluene, we performed ECD calculations employing different functionals, namely B3LYP/6-31G(d,p), CAM-B3LYP/6-31G(d,p), M06/TZVP, and LC-wPBE/6-31g(d,p). As a result, indeed 100 transition calculation rendered the theoretical two first less energetic bands with coincident sign as the experimental ones. Regarding the energy of the transitions, in both **mPTM** and **bPTM** cases, they were better reproduced at the M06/TZVP level of theory, and B3LYP/6-31G(d,p), whilst CAM-B3LYP/6-31G(d,p) and LC-wPBE/6-31G(d,p) performed slightly better for the intensity of the bands, specially CAM-B3LYP/6-31G(d,p) (**Figure S3.3**).

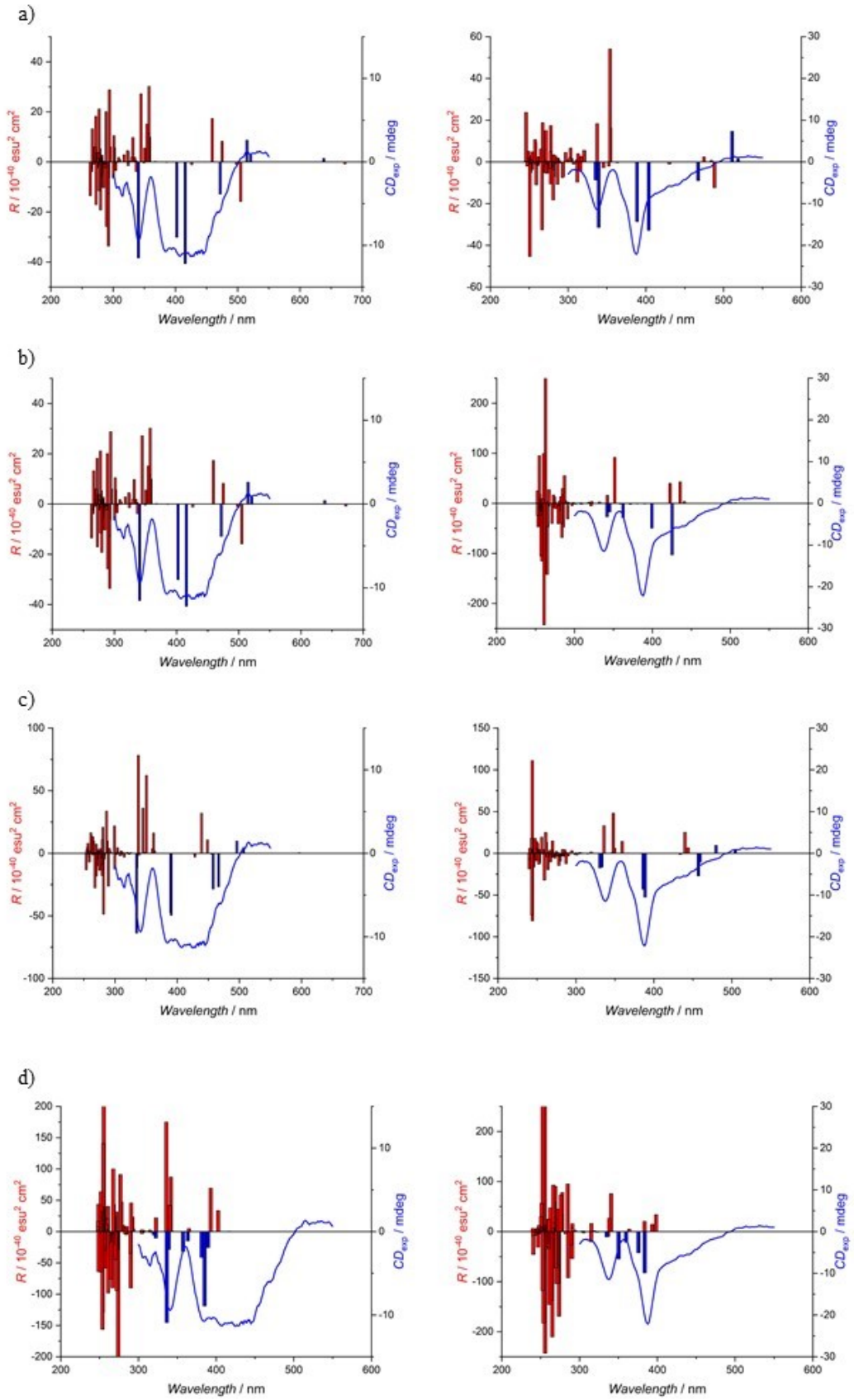

Figure S3.3. Theoretical ECD spectra of ***(P)*-bPTM** (left) and ***(P)*-mPTM** (right) at the a) B3LYP/6-31G(d,p), b) CAM-B3LYP/6-31G(d,p), c) M06/TZVP, and d) LC-wPBE/6-31G(d,p) level of calculation. Theoretically calculated R were batochromically shifted 50-60 nm to better match the

experimental ECD in cases b) and d). Blue R columns mark coincident theoretical-experimental matching.

Cartesian coordinates and corresponding total energies for optimized geometries

***(M)*-mPTM** B3LYP/6-31G(d,p)

C	-1.28607000	-0.01226800	0.00806300
C	-2.15992000	-1.20884900	-0.01333100
C	-3.20547300	-1.35186500	-0.95870300
C	-1.99232500	-2.26736500	0.91396500
C	-4.04248500	-2.47562300	-0.97494300
C	-2.80853400	-3.40633900	0.89422500
C	-3.84203700	-3.51112700	-0.04925700
C	0.18248800	-0.16806100	0.03978900
C	0.99178700	0.53678000	0.96730200
C	0.86313200	-1.03218200	-0.85503100
C	2.38567100	0.40573800	0.98664400
C	2.25244000	-1.17018600	-0.82017700
C	3.06044800	-0.44671800	0.08504200
C	-1.88849500	1.34124900	-0.00214700
C	-1.45660800	2.33938100	-0.91106900
C	-2.92545500	1.70309000	0.89331900
C	-2.01435000	3.62506200	-0.91998600
C	-3.50688700	2.97810700	0.87900800
C	-3.04743500	3.94682300	-0.02641800
Cl	-0.80932800	-2.13442700	2.18590400
Cl	-2.57051700	-4.68181500	2.04928000
Cl	-4.86460100	-4.91050200	-0.07064100
Cl	-5.31257200	-2.61314700	-2.15193700
Cl	-3.41949600	-0.15816200	-2.20986400
Cl	0.23368900	1.50969700	2.20255300
Cl	3.29437900	1.24940400	2.21959100
Cl	3.04317500	-2.21884600	-1.97558000
Cl	-0.02161600	-1.85951100	-2.11051000
Cl	-3.44694700	0.58413000	2.12283800
Cl	-4.77564700	3.38206900	1.99452700
Cl	-0.26771300	1.95927800	-2.12690900
Cl	-1.45686300	4.82074800	-2.05014300
Cl	-3.75125900	5.53090100	-0.04061900
C	4.51604100	-0.65527600	0.06747900
H	4.81994300	-1.69002100	-0.05472700
C	5.45311000	0.31267700	0.10048700
H	5.13320600	1.35026100	0.13988800
C	6.90315000	0.11982400	0.04874000
C	7.72855500	1.25321700	-0.07811800
C	7.52396500	-1.14349500	0.12315100
C	9.11123000	1.13898900	-0.14120400
H	7.27224800	2.23765900	-0.13177100
C	8.90339900	-1.26679900	0.06181100
H	6.92391300	-2.03984900	0.24062100
C	9.72260200	-0.12647700	-0.07371900
H	9.72920800	2.02480700	-0.24158100
H	9.36540700	-2.24644600	0.12239000
C	11.14319000	-0.25582400	-0.13651500
C	12.34784700	-0.36727100	-0.19031300

H	13.40855500	-0.46456100	-0.23768400

Zero-point correction = 0.263763 (Hartree/Particle)
Thermal correction to Energy = 0.305483
Thermal correction to Enthalpy = 0.306428
Thermal correction to Gibbs Free Energy = 0.181176
Sum of electronic and zero-point Energies = -7551.605171
Sum of electronic and thermal Energies = -7551.563451
Sum of electronic and thermal Enthalpies = -7551.562507
Sum of electronic and thermal Free Energies = -7551.687759

***(M)*-bPTM** B3LYP/6-31G(d,p)

C	-0.01152800	1.16969600	0.03174400
C	-1.36477300	0.57753400	0.06032000
C	-2.37540500	0.96849000	-0.85399200
C	-1.72643300	-0.41760300	1.00458000
C	-3.64655800	0.39032400	-0.82740600
C	-2.99762800	-1.00452600	1.01531900
C	-3.99462700	-0.62636700	0.08922200
C	1.18006700	0.29484400	0.05337900
C	2.25845500	0.51464600	0.94746200
C	1.30816400	-0.81491000	-0.81987400
C	3.39441500	-0.30404300	0.95825700
C	2.43669900	-1.63731100	-0.79285600
C	3.52139100	-1.40330100	0.08104300
C	0.15416500	2.64127200	-0.02106600
C	1.00042000	3.26045000	-0.97408700
C	-0.52373500	3.49998600	0.87939700
C	1.17353000	4.65023100	-1.02031800
C	-0.37483300	4.89257300	0.83028600
C	0.48107500	5.47241800	-0.11847100
Cl	-0.60257000	-0.85146500	2.26780900
Cl	-3.37939500	-2.16517300	2.26698600
Cl	-4.84072900	0.88043600	-2.00856200
Cl	-2.00993000	2.10829100	-2.12353900
Cl	2.12945900	1.76778700	2.15569600
Cl	4.63648000	-0.00554200	2.15297400
Cl	2.55888800	-2.97040500	-1.91978700
Cl	0.09513300	-1.11049100	-2.03887100
Cl	-1.50348300	2.82931600	2.15481100
Cl	-1.22057000	5.91096000	1.95573300
Cl	1.78494400	2.30012500	-2.19839000
Cl	2.21876100	5.37053000	-2.20684100
Cl	0.68128800	7.19379900	-0.17661200
C	4.66788900	-2.32480200	0.06104900
H	4.39960800	-3.37296300	-0.02675000
C	5.96774100	-1.97001800	0.05746300
H	6.22271100	-0.91389100	0.06263200
C	7.11534100	-2.87758700	0.00880500
C	8.40022000	-2.32949800	-0.16595500
C	7.00717800	-4.27736500	0.13399400
C	9.52972400	-3.13537300	-0.22660500
H	8.50848000	-1.25249100	-0.25885900

C	8.12932700	-5.08937900	0.07573100
H	6.03692300	-4.73741500	0.28996400
C	9.41218700	-4.53241900	-0.10764300
H	10.51045800	-2.69282400	-0.36447400
H	8.02853800	-6.16485000	0.17616600
C	10.56676400	-5.37038400	-0.16628500
C	11.54534900	-6.08198500	-0.21669700
H	12.40715900	-6.70816700	-0.26082500
C	-5.35481500	-1.18517000	0.05508500
H	-6.13960100	-0.45149000	-0.09893700
C	-5.67161600	-2.49395800	0.10544700
H	-4.87085200	-3.22500800	0.17443400
C	-7.01799700	-3.06397000	0.03341200
C	-7.15204000	-4.45926600	-0.09699800
C	-8.19495800	-2.29047200	0.08989900
C	-8.40028500	-5.06204700	-0.18275700
H	-6.25829600	-5.07570600	-0.13626000
C	-9.44515000	-2.88390000	0.00647000
H	-8.13420700	-1.21392300	0.21156300
C	-9.57019800	-4.28183100	-0.13417900
H	-8.48176900	-6.13875700	-0.28639100
H	-10.34122900	-2.27424400	0.05369900
C	-10.85853900	-4.89136300	-0.22004400
C	-11.95147500	-5.40773400	-0.29342200
H	-12.91367200	-5.86242900	-0.35815800

Zero-point correction = 0.396384 (Hartree/Particle)
Thermal correction to Energy = 0.446132
Thermal correction to Enthalpy = 0.447076
Thermal correction to Gibbs Free Energy = 0.302669
Sum of electronic and zero-point Energies = -7476.499858
Sum of electronic and thermal Energies = -7476.450111
Sum of electronic and thermal Enthalpies = -7476.449167
Sum of electronic and thermal Free Energies = -7476.593573

***(M)*-bPTM** B3LYP/6-311G+(d,p)

C	-0.01160500	1.16781200	0.03439000
C	-1.36450600	0.58286200	0.06461200
C	-2.37184600	0.97891000	-0.84638900
C	-1.72749500	-0.40863300	1.00760300
C	-3.64273400	0.40775200	-0.81847400
C	-2.99841900	-0.98860000	1.02002200
C	-3.99160600	-0.60578700	0.09631100
C	1.17358600	0.28945200	0.05984000
C	2.25059300	0.50960800	0.95056400
C	1.29423800	-0.82302500	-0.80585600
C	3.37981700	-0.31293000	0.96537400
C	2.41636100	-1.64879100	-0.77572800
C	3.49963900	-1.41413000	0.09445300
C	0.16060300	2.63502400	-0.02301500
C	1.01351600	3.24461900	-0.97170700
C	-0.51742100	3.49781800	0.86857600
C	1.19280700	4.63004800	-1.02233600

C	-0.36109200	4.88605200	0.81626500
C	0.50120200	5.45672900	-0.12823600
Cl	-0.60619200	-0.83894700	2.27471500
Cl	-3.38697700	-2.14381400	2.27469900
Cl	-4.83769800	0.90183200	-1.99673400
Cl	-1.99959400	2.11245600	-2.11976000
Cl	2.12310700	1.76573400	2.15615800
Cl	4.62185700	-0.01957400	2.16143600
Cl	2.53407400	-2.98804600	-1.89530900
Cl	0.08213700	-1.11233400	-2.02759900
Cl	-1.50253900	2.83422300	2.14416900
Cl	-1.20707600	5.91219000	1.93451100
Cl	1.79281300	2.27507800	-2.19272000
Cl	2.24721900	5.34074600	-2.20656200
Cl	0.71084600	7.17673600	-0.19077400
C	4.64520800	-2.33682400	0.07728600
H	4.37646400	-3.38566800	0.02405100
C	5.93998600	-1.97957400	0.04310400
H	6.19129000	-0.92412200	0.02196700
C	7.09127700	-2.88237000	-0.00401600
C	8.37205000	-2.33008600	-0.17726900
C	6.98998500	-4.28047100	0.12036900
C	9.50438800	-3.13032300	-0.23515800
H	8.47691400	-1.25452100	-0.27021500
C	8.11467200	-5.08619700	0.06499900
H	6.02374600	-4.74677200	0.27041000
C	9.39360900	-4.52489400	-0.11545900
H	10.48117800	-2.68268800	-0.37155600
H	8.01743300	-6.16044200	0.16433000
C	10.55073500	-5.35672500	-0.17130200
C	11.52846800	-6.06083600	-0.21936600
H	12.39112800	-6.68126800	-0.26145900
C	-5.35237400	-1.16326700	0.06334000
H	-6.13857200	-0.42743500	-0.05983800
C	-5.66327700	-2.47033200	0.08628200
H	-4.86024600	-3.19875500	0.13107300
C	-7.00721800	-3.04620700	0.01738700
C	-7.13559300	-4.43964500	-0.11400200
C	-8.18603900	-2.27999100	0.07812400
C	-8.38045700	-5.04760400	-0.19483900
H	-6.24141600	-5.05211000	-0.15715600
C	-9.43214300	-2.87866400	-0.00008200
H	-8.13232300	-1.20444300	0.19612300
C	-9.55156800	-4.27487200	-0.14045200
H	-8.45571700	-6.12307300	-0.29865100
H	-10.32884900	-2.27311500	0.05039600
C	-10.83595300	-4.88967900	-0.22056500
C	-11.92216800	-5.40880700	-0.28901700
H	-12.87999800	-5.86687000	-0.34919200

Zero-point correction = 0.394562 (Hartree/Particle)
Thermal correction to Energy = 0.444446
Thermal correction to Enthalpy = 0.445390
Thermal correction to Gibbs Free Energy = 0.300432

Sum of electronic and zero-point Energies = -7477.210579
Sum of electronic and thermal Energies = -7477.160694
Sum of electronic and thermal Enthalpies = -7477.159750
Sum of electronic and thermal Free Energies = -7477.304708

4. Enantiomerization barrier calculation

Based on the reversibility of the enantiomerization process, the thermodynamic parameters can be calculated using the equation of Eyring-Polanyi (**Equation S3**) and Gibbs equation (**Equation S5**).[3,4]

$$ln\frac{k_e}{T} = -\frac{\Delta H^{\ddagger}}{RT} + ln\frac{\kappa k_B}{h} + \frac{\Delta S^{\ddagger}}{R} \qquad \textbf{Equation S3}$$

$$2k_e = k_{rac} \qquad \textbf{Equation S4}$$

k_{rac}=kinetic constant of the racemization process.

k_e=kinetic constant of the enantiomerization process.

$$\Delta G^{\ddagger} = \Delta H^{\ddagger} - T\Delta S^{\ddagger} \qquad \textbf{Equation S5}$$

where k_B is the Boltzmann constant (1.38x10^{-23} J/K), h is Planck constant (6.63x10^{-34} J s), R is the ideal gas constant (1.98x10^{-3} kcal mol^{-1} K^{-1}), T is the temperature (in K), $\Delta H^{\ddagger}$ is the activation enthalpy (in kcal/mol^{-1}), $\Delta S^{\ddagger}$ is the activation entropy (in kcal/mol K) and κ is the transition coefficient for a reversible reaction with a value of 0.5.

Experimentally, it is possible to determine k_{rac} at different temperatures following the enantiomeric excess (ee), e.g. by liquid chromatography. The decay is fitted assuming a first order kinetic reaction (**Equation S6**). Having determined k_{rac} values, k_e is calculated using **Equation S4**[3,4]

$$\ln [ee] = -k_{rac}t \qquad \textbf{Equation S6}$$

Using ECD, we can follow the decay of the ratio between the value of the maximum peak at a certain wavelength of the ECD spectrum at a given time (ECD_t) and the one for the ECD at t = 0 (ECD_0) which is proportional to the enantiomeric excess (**Equation S7)**.

$$\ln\left[\frac{ECD_t}{ECD_0}\right] = -k_{rac}t \qquad \textbf{Equation S7}$$

Based on **Equation S7**, we followed the exponential decay of the signal at 387 nm in a temperature range of 278 K to 298 K for ***(M)*** conformers of both radicals **mPTM** and **bPTM** (**Figure S4**). The decay was fitted using a first-order kinetic equation (see **Equation S7**) to obtain the kinetic constants k_{rac} and then, k_e was calculated using **Equation S4**.

Table S1 summarizes the extracted values for both molecules.

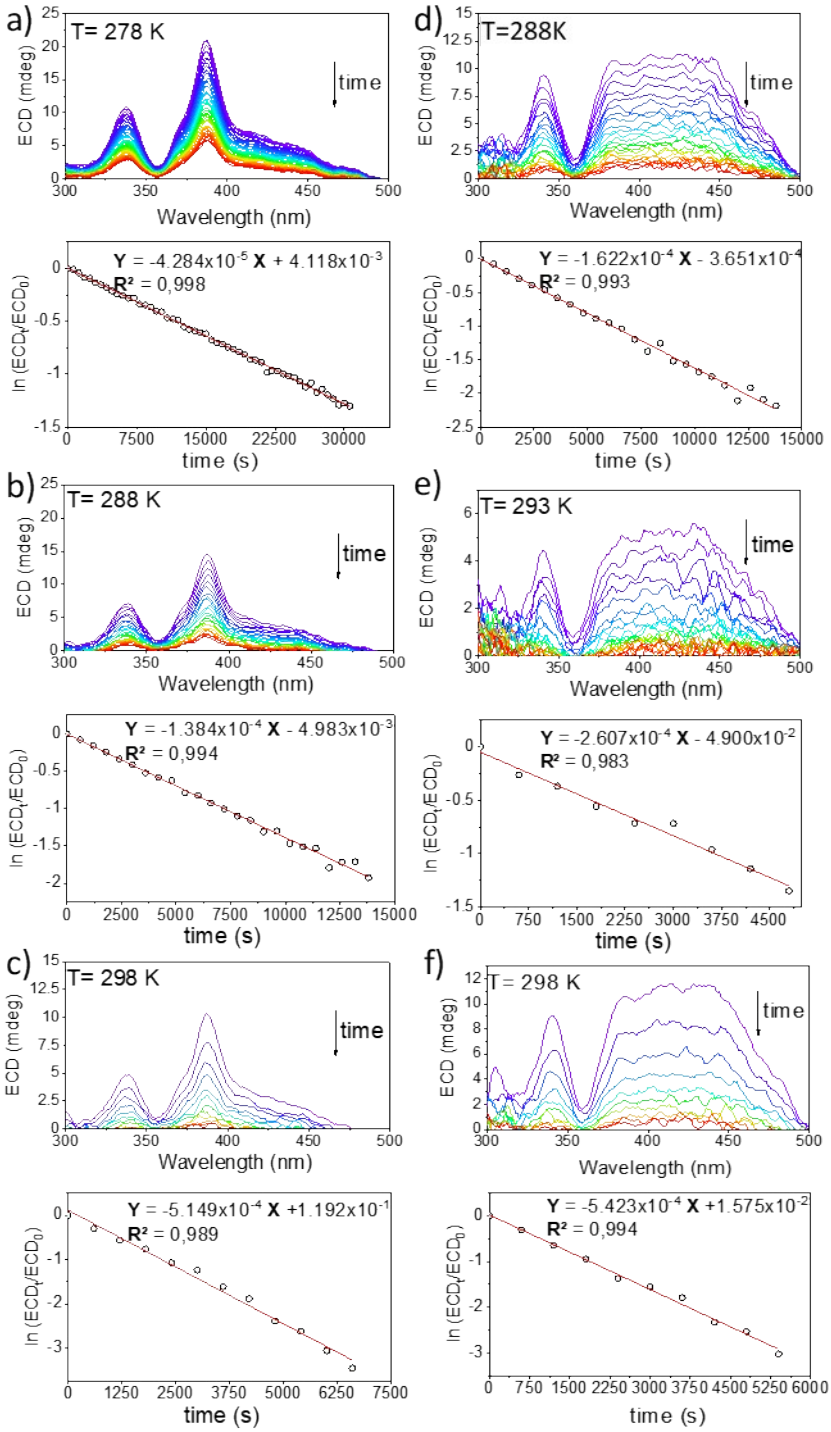

Figure S4. a), b) and c) Top: ECD signal decay for ***(M)*-mPTM** at 278, 288 and 298 K, in toluene. The time increase from purple to red. Bottom: Linear fitting of $\ln(ECD_t/ECD_0)$ signal decay assuming a first

order kinetic for ***(M)*-mPTM** at 387 nm. d), e) and f) Top: ECD signal decay of ***(M)*-bPTM** at 288, 293 and 298 K, in toluene. Bottom: Linear fitting of the $\ln(ECD_t/ECD_0)$ signal decay assuming a first order kinetic of ***(M)*-bPTM** at 387 nm.

To corroborate the obtained values from the ECD experiments, the kinetic parameters of the racemization were also estimated using (CSP)-HPLC. For these experiments, the samples of ***(P)***-enantiomers were heated *ex-situ* in a temperature range of 278 K to 293 K and, later injected into the chromatograph to determine the ee. The ee values for ***(P)*** enantiomers were extracted as described above (**Equation S1 and Equation S2**) and the decay was fitted assuming a first-order kinetic **Figure S5**).

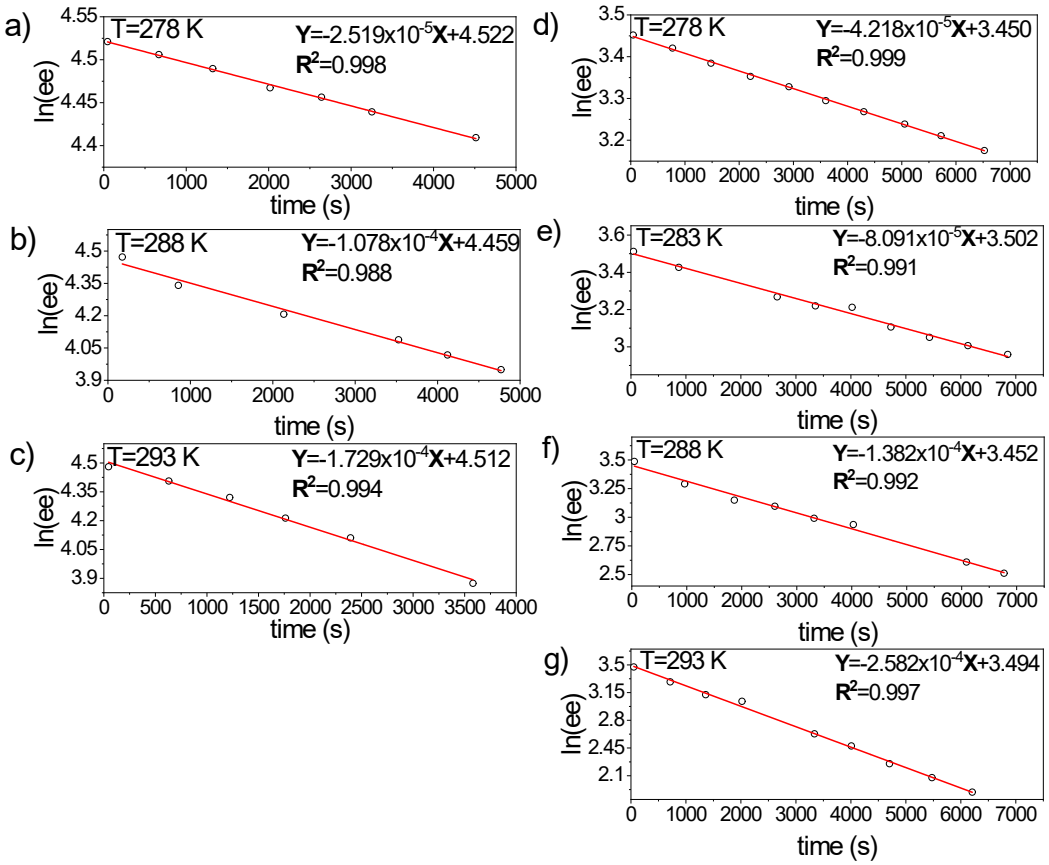

Figure S5. Linear fitting of the ee values decay measured by (CSP)-HPLC assuming a first-order kinetic for ***(P)*-mPTM** at a) 278 K, b) 288 K and c) 293 K and for ***(P)*-bPTM** at d) 278 K, e) 283 K, f) 288 K and g) 293 K.

The half-life time ($t_{1/2}$) for the racemization process was determined using **Equation S8** and the associated error using **Equation S9.** The results are summarized in **Table S1**. Clearly, the temperature rise results in an increment of the k_{rac} and hence, a decrease of the half-life time of the racemization.

$$t_{1/2} = \frac{ln(2)}{k_{rac}} \qquad \textbf{Equation S8}$$

$$\delta t_{1/2} = t_{1/2} \cdot \left(\frac{\delta k_{rac}}{k_{rac}} \right) \qquad \textbf{Equation S9}$$

Table S1 Kinetic constants of the racemization (krac) and enantiomerization (ke) processes and half-life time ($t_{1/2}$). Determined via the decay of the ECD signal or via (CSP)-HPLC, for radicals **mPTM** and **bPTM**.

Compound and method	T (K)	k_{rac} (s^{-1}) x10^{-4}	k_e (s^{-1}) x10^{-4}	$t_{1/2}$ (h)
***(M)*-mPTM (ECD)**	278	0.430±0.003	0.215±0.001	4.48±0.03
	288	1.38±0.02	0.69±0.01	1.40±0.02
	298	5.2±0.2	2.6±0.1	0.37±0.01
***(M)*-bPTM (ECD)**	288	1.62±0.03	0.81±0.02	1.19±0.02
	293	2.6±0.1	1.31±0.06	0.74±0.03
	298	5.4±0.1	2.71±0.07	0.35±0.01
***(P)*-mPTM (CSP)-HPLC**	278	0.252±0.005	0.126±0.003	7.6±0.2
	288	1.08±0.06	0.54±0.03	1.8±0.1
	293	1.73±0.07	0.865±0.04	1.11±0.05
***(P)*-bPTM (CSP)-HPLC**	278	0.422±0.004	0.209±0.002	4.56±0.04
	283	0.81±0.02	0.40±0.01	2.38±0.06
	288	1.38±0.05	0.691±0.03	1.40±0.05
	293	2.58±0.05	1.29±0.03	0.75±0.01

The enthalpy (ΔH) and entropy (ΔS) of the enantiomerization process were calculated through a linear fit (**Figure S6**) of ln(k_e/T) *versus* 1/T, based on Eyring-Polanyi equation (**Equation S3**). In addition, the racemization barrier was estimated using Gibbs equation (**Equation S5**), while the $\Delta G^{\ddagger}$ errors ($\delta\Delta G^{\ddagger}$) were determined using error propagation from the slope (δb) and intercept error (δa) of the linear fit (**Equation S10 and Equation S11** Assuming a linear equation y=bx+a; the slope and intercept of the plot ln(k_e/T) *versus* 1/T, based on Eyring-Polanyi equation, are:

$$b = -\frac{\Delta H^{\ddagger}}{R} \quad \text{and} \quad a = ln\frac{\kappa k_B}{h} + \frac{\Delta S^{\ddagger}}{R} \qquad \textbf{Equation S10}$$

$$\delta\Delta H^{\ddagger} = \delta b \cdot R \quad \text{and} \quad \delta\Delta S^{\ddagger} = \delta a \cdot R \qquad \textbf{Equation S11}$$

$$\delta\Delta G^{\ddagger} = \sqrt{[\delta\Delta H^{\ddagger}]^2 + T^2[\delta\Delta S^{\ddagger}]^2} \qquad \textbf{Equation S12}$$

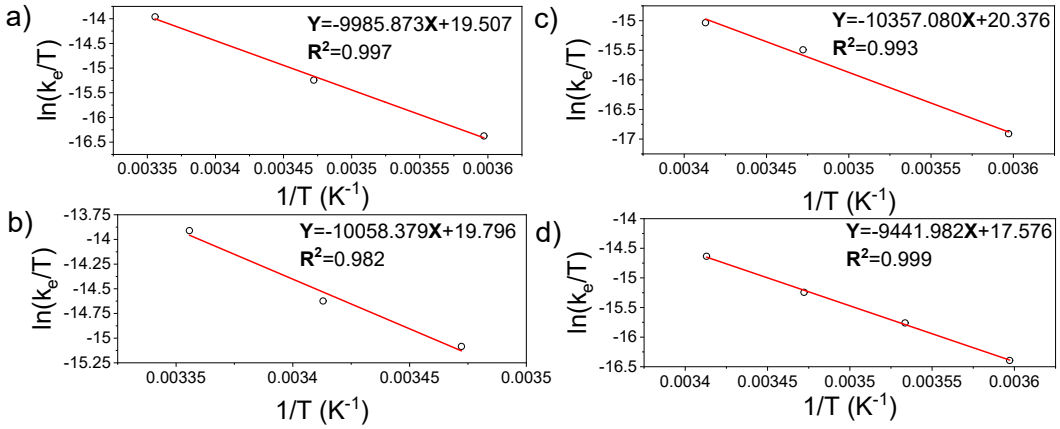

Figure S6. Eyring-Polanyi plots and linear fits for a) ***(M)*-mPTM** (kinetic constant extracted *via* the decay of the ECD intensity) b) ***(M)*-bPTM** (kinetic constant extracted *via* the decay of the ECD intensity) c) ***(P)*-mPTM** (kinetic constant extracted *via* (CSP)-HPLC) and d) ***(P)*-bPTM** (kinetic constant extracted *via* (CSP)-HPLC).

Table S2. Thermodynamic data of the enantiomers ***(M)*-mPTM**, ***(P)*-mPTM**, ***(M)*-bPTM** and ***(P)*-bPTM** calculated from Eyring and Gibbs equations.

Compound and method	$\Delta H^{\ddagger}$ (kcal/mol)	$\Delta S^{\ddagger}$ (kcal/mol)	$\Delta G^{\ddagger}_{(298\ K)}$ (kcal/mol)
***(M)*-mPTM (ECD)**	20±1	-0.007±0.004	22±2
***(M)*-bPTM (ECD)**	20±3	-0.007±0.009	22±4
***(P)*-mPTM (CSP)-HPLC)**	21±2	-0.005±0.006	22±3
***(P)*-bPTM ((CSP)-HPLC)**	19±1	-0.011±0.002	22±1

5. Film Characterization

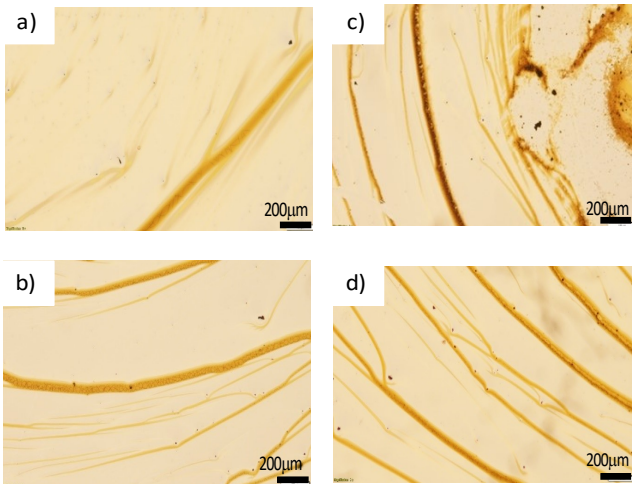

Figure S7. Representative optical microscopy images of the enantioenriched films deposited by drop-casting on Quartz/Ti/Au substrate: a) ***(P)*-mPTM**, b) ***(M)*-mPTM**, c) ***(P)*-bPTM** and d) ***(M)*-b-PTM**.

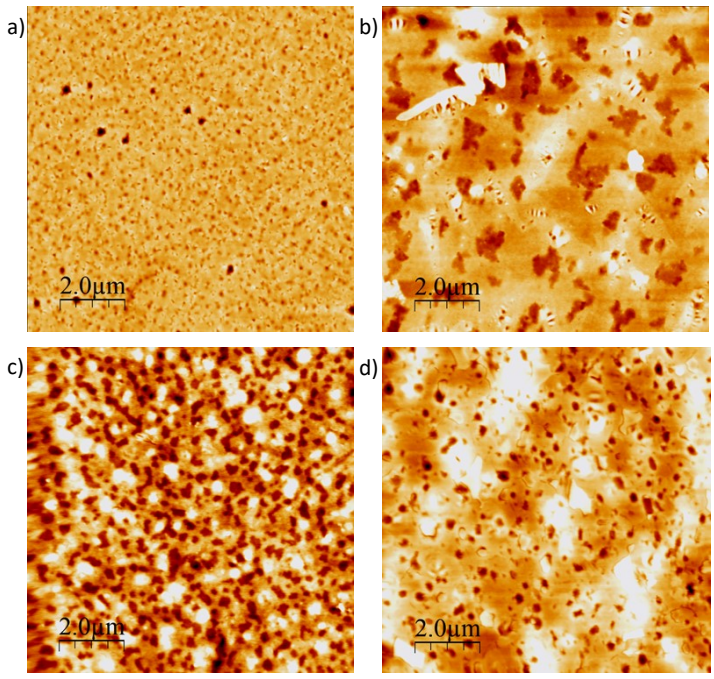

Figure S8. Topographic tapping-AFM images of the enantioenriched films deposited by drop-casting on Quartz/Ti/Au substrate of a) ***(P)*-mPTM**, b) ***(M)*-mPTM**, c) ***(P)*-bPTM** and d) ***(M)*-bPTM**.

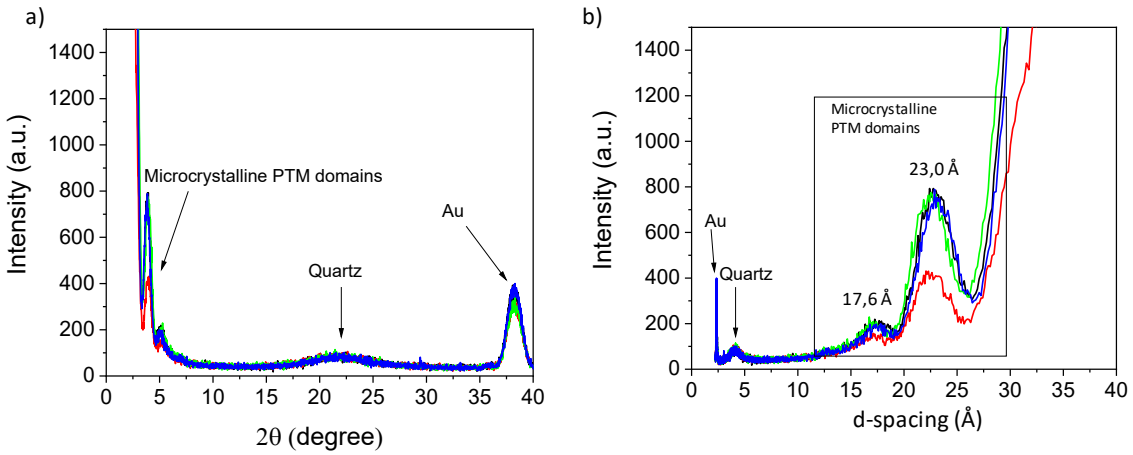

Figure S9. a) XRD diffractograms of the enantioenriched films deposited by drop-casting on Au/quartz of ***(P)*-mPTM** (red), ***(M)*-mPTM** (black), ***(P)*-bPTM** (blue) and ***(M)*-bPTM** (green); b) *d-spacing* plot.

Clear peaks around 22º and 38º are attributed to the quartz and gold substrate respectively. Additionally, at very low angles (4-5 º), we observed two peaks which could be attributed to microcrystalline structures on the gold surface associated with the PTM thin film. However, due to the lack of single crystal data, we could not assign these peaks.

Table S3. Comparison of the absorption peaks position (A_p) of compounds **mPTM** and **bPTM** in solution and in thin films.

	A_p in solution (nm)	**A_p in film (nm)**	**ΔAbs (nm)**
mPTM	309	317	8
	386	395	9
	441	459	18
bPTM	310	318	8
	380	385	5
	445	465	20

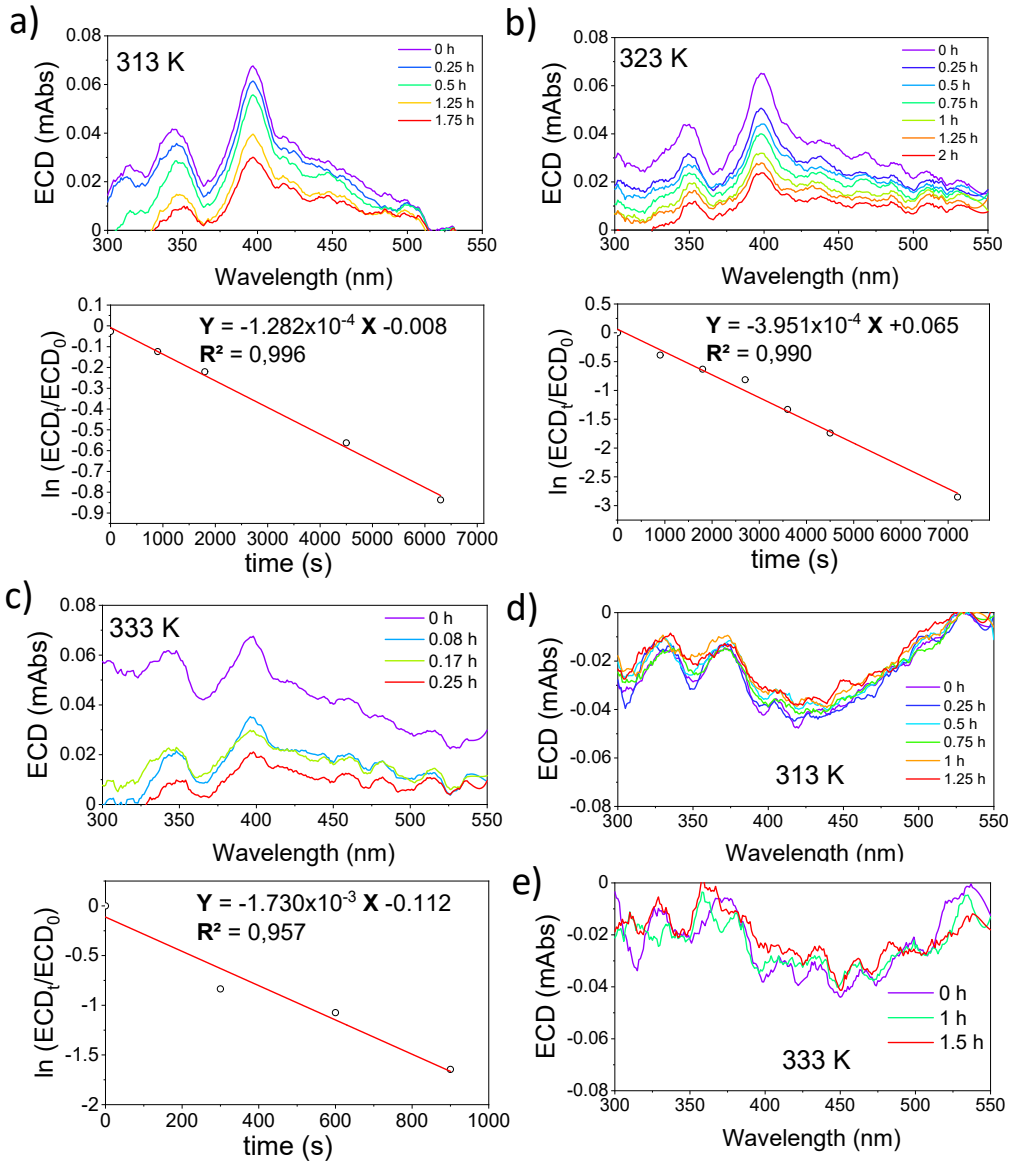

Figure S10. Top: ECD spectra and Bottom: linear fittings of the $\ln(ECD_t/ECD_0)$ signal decay (398 nm) assuming a first order kinetic for the ***(M)*-mPTM-film** at: a) 313 b) 323 and c) 333 K. ECD spectra of the ***(P)*-bPTM-film** at d) 313 K and e) at 333 K.

Table S4. Kinetic constants of the racemization (k_{rac}) and enantiomerization (k_e) processes determined *via* ECD for ***(M)*-mPTM** film.

	Temperature (K)	k_{rac} (s^{-1}) x10^{-4}	k_e (s^{-1}) x10^{-4}	$t_{1/2}$ (h)
***(M)*-mPTM film**	313	1.28±0.04	0.64±0.02	1.50±0.05
	323	4.0±0.2	2.0±0.1	0.48±0.02
	333	17±3	9±1	0.11±0.02

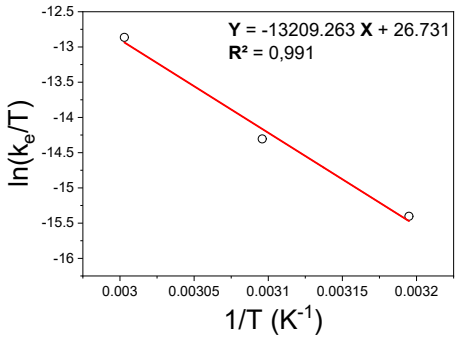

Figure S11. Eyring-Polanyi plot and linear fit for the ***(M)*-mPTM-film** (kinetic constant extracted *via* the decay of the ECD intensity).

$$\Delta G^{\ddagger}_{min} = -RT ln\left(\frac{k_e\, h}{\kappa k_B T}\right) \qquad \textbf{Equation S13}$$

6. Preparation of the monolayer

7.1-General considerations

All the glassware used for the preparation of SAMs was first cleaned following standard procedures and then further washed by overnight immersion in a 2 % v/v Hellmanex II solution in MilliQ water, thoroughly rinsed with MilliQ water, and dried in an oven at 80 ºC overnight. The solvents used for the substrates cleaning and SAMs rinsing were always of HPLC grade.

7.2-Procedure for racemic and enantioenriched SAMs preparation

To form the SAMs, the freshly prepared substrates (Au/quartz or Au/Ni) were introduced into a flat bottom flask. The flask was degassed by performing several argon-vacuum cycles and kept cold in a freezer (-18 ºC). A 1 mM toluene solution of the desired compound (***(RAC)*-bPTM**, ***(M)*-bPTM** or ***(P)*-bPTM**) previously degassed and cooled (-18 ºC) was introduced in the flask containing the

substrates. The solution was kept for 48 h at -18 ºC in dark. After the incubation time, the substrates were removed from the solution and rinsed with cold toluene. The scheme of all the SAMs prepared in this work are shown in **Figure S12**.

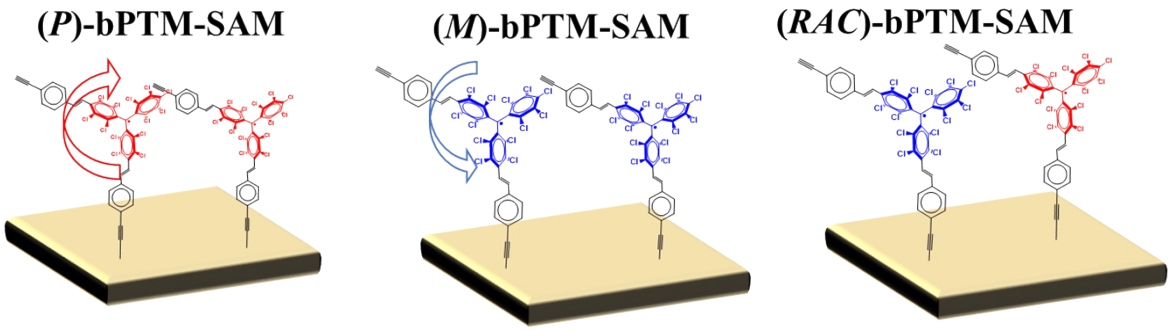

Figure S12. Schematic representation of the **bPTM** SAMs.

7.3-Substrates preparation for the SAMs formation

Semi-transparent Gold substrates: Rough semitransparent Au surfaces were prepared by sequential thermal depositions of Ti (2 nm) and Au (6 nm) on quartz coverslip, 19 x 19 mm^2 or 9.5 x 9.5 mm^2, 0.5 mm thick (TED PELLA, INC. 26016). The deposition parameters were 4 x 10^{-7} mTorr and a rate of 0.2 Å/s. The substrates were used immediately after their preparation and without any further cleaning procedure.

Nickel-Gold substrates (NiAu): Rough ferromagnetic substrates were prepared using the methodology reported by P. C. Mondal.[5] Sequential thermal depositions of Ti (5 nm), Ni (185 nm) and finally Au (10 nm) were performed on silicon wafer pieces with 50 nm of silicon oxide. The top Au layer was added to avoid the oxidation of the underneath Ni surface. The deposition parameters were 4 x 10^{-7} mTorr and rate 0.2 Å/s for the first 20 nm and then 2 Å/s. The substrates were used immediately after their preparation and without any further cleaning procedure.

Nickel-Gold template-stripped ($NiAu^{TS}$) substrates: Ultra-smooth template-striped gold substrates were prepared based on a reported procedure.[6,7] It basically consists in the thermal deposition of Au (10 nm)/Nickel (200 nm)/Au (10 nm) on a silicon (100) wafer with its native SiO_2 surface layer. The deposition parameters were 4 x 10^{-7} mTorr and a rate 0.2 Å/s for the first 20 nm and then increased to 2 Å/s for the rest. After the metal deposition, several glass slides (of different sizes) were glued onto the exposed gold using an epoxy resin (EpoTek, 353ND). The adhesive was cured in an oven (temperature ramp: 3 h (0 to 60 ºC), 12 h (60 ºC) and 3 h (60 ºC to 0 ºC)). The glass/epoxy/metal substrate was cleaved from the Si wafer just before immersion into the desired solution to minimize the contamination from air, and without any further cleaning procedure (**Figure S13**).

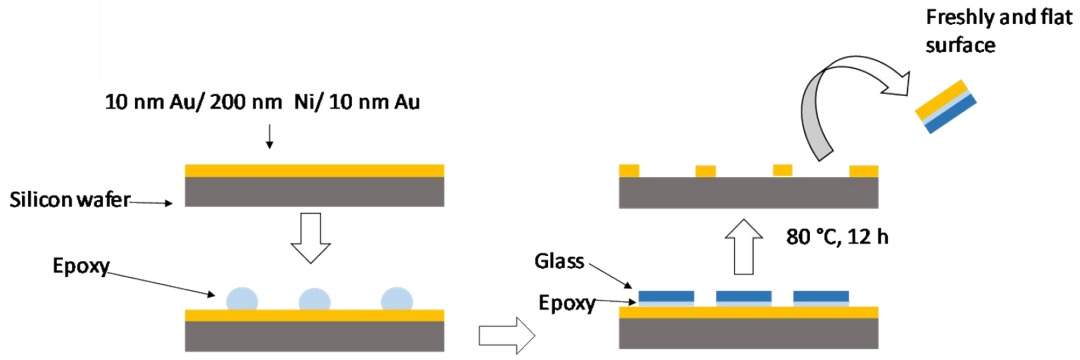

Figure S13. Schematic procedure for the preparation of NiAu template-stripped substrates.

7. Monolayer characterization

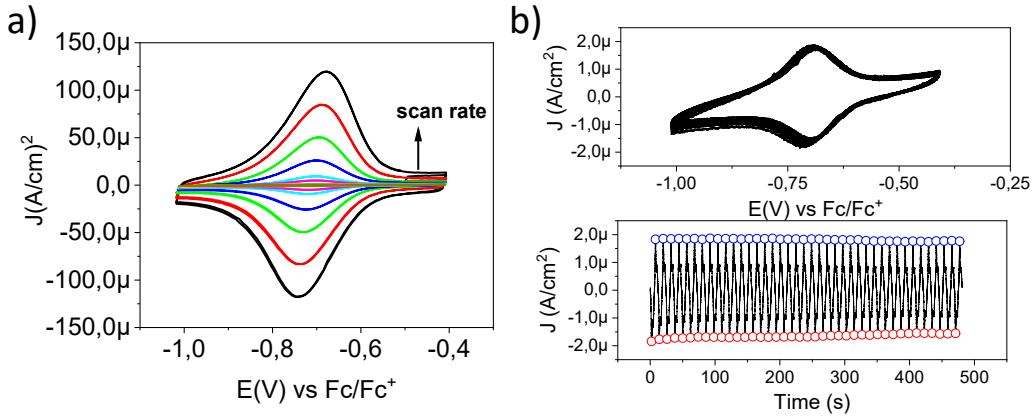

Figure S14. Cyclic voltammograms of ***(RAC)*-bPTM-SAM** in CH_2Cl_2 + 0.2 M Bu_4NPF_6 at different scan rates (0.05, 0.1, 0.25, 0.5, 1, 2, 3 and 4 V/s) under argon atmosphere. b) Top: Cyclic voltammogram (40 scans) at 0.1 V/s, Bottom: Current density at the anodic and cathodic peak (J_{pa} (Blue), J_{pc} (Red)) as a function of time of ***(RAC)*-bPTM-SAM** in CH_2Cl_2 + 0.2 M Bu_4NPF_6. WE=SAMs/Au, RE= Ag/AgCl KCl 3 M (plotted *vs.* Fc/Fc^+ couple), CE= Pt Mesh.

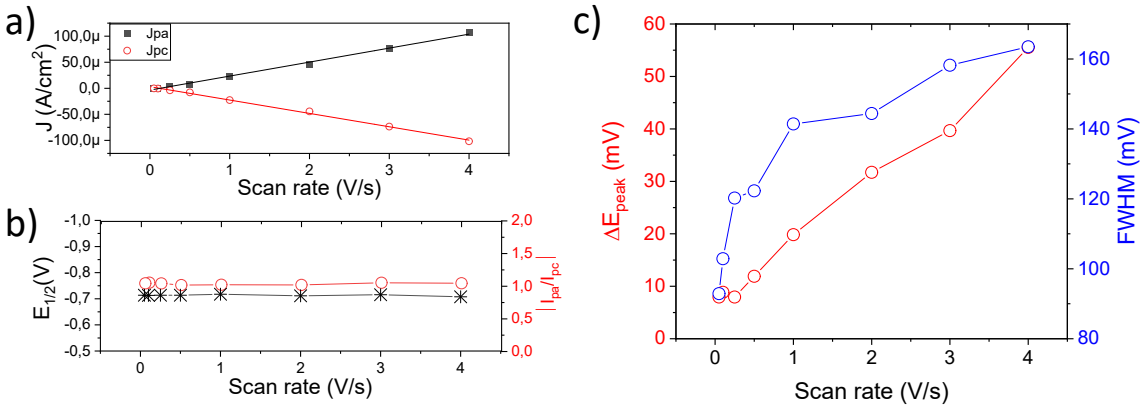

Figure S15. Reversibility plots analysis for ***(RAC)*-bPTM-SAM**. a) Anodic and cathodic current densities (J_{pa} and J_{pc}) *versus* scan rate. b) $E_{1/2}$ (black) and $|I_{pa}/I_{pc}|$ (red) *versus* scan rate. c) ΔE_{peak} (red) and FWHM (blue) *versus* scan rate.

8.1-Surface Coverage Calculation

The surface coverage was calculated from the Equation S14[8,9]:

$$\Gamma = \frac{A_{peak}}{nFSv}$$

Equation S14

where Γ is the surface coverage in mol cm^{-2}, A_{peak} is the integrated area of the anodic or cathodic voltammetry peak, n is the number of electrons transferred (in this case n = 1), F is Faraday's constant, S is the electrode surface area and v is the potential scan rate.

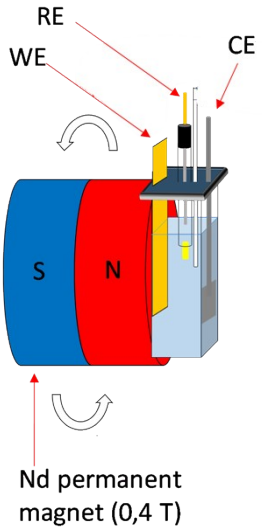

Figure S16. Scheme of the custom-built electrochemical cell used to perform spin-dependent cyclic voltammetry.

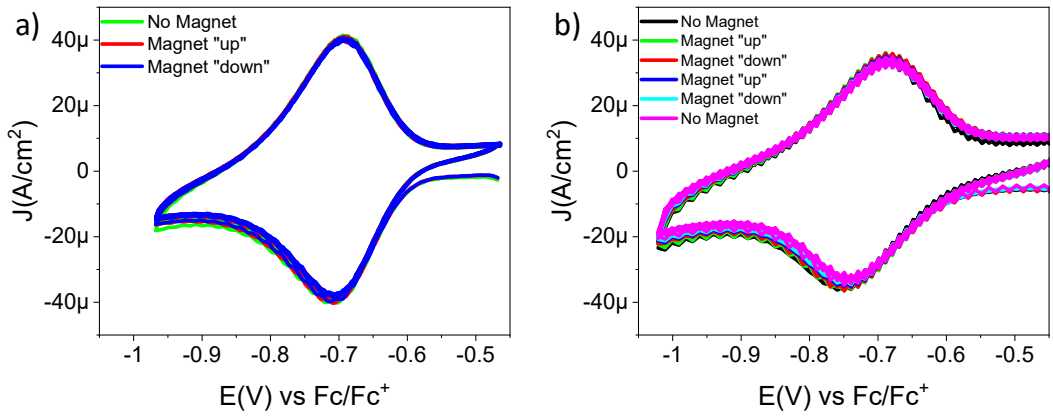

Figure S17. Spin-dependent cyclic voltammetry of a) ***(RAC)*-bPTM-SAM** and b) ***(P)*-bPTM-SAM** in CH_2Cl_2 + 0.2 M Bu_4NPF_6 at 1 V/s under argon atmosphere. WE=SAMs/Au, RE=Ag wire (pseudo-

reference), internal reference Fc/Fc^+ couple, CE= PT Mesh. Magnetization time: 60 seconds before the cyclic voltammetry.

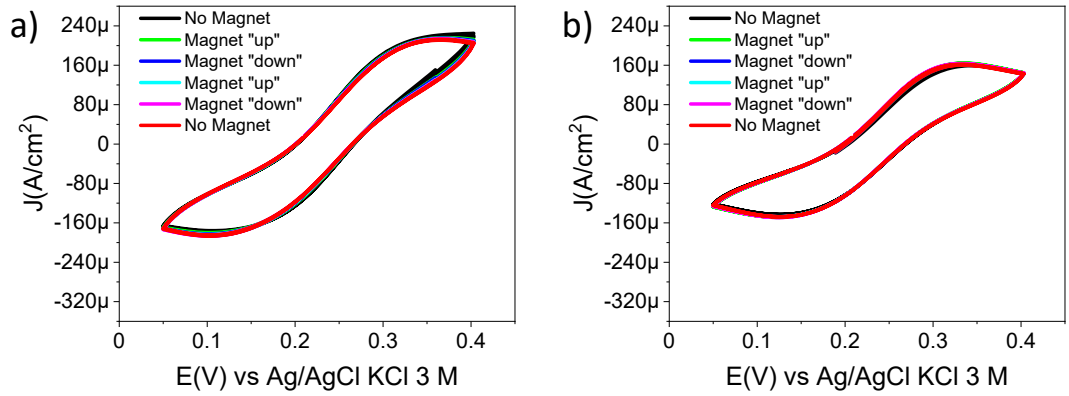

Figure S18. Spin-dependent cyclic voltammetry of a) ***(P)*-bPTM-SAM** at 0.1 V/s and b) ***(P)*-bPTM-SAM** at 0.05 V/s using $K_4Fe(CN)_6$ (1 mM)/$K_3Fe(CN)_6$ (1 mM) as redox proof in KCl 0.1 M, under argon atmosphere. WE=SAMs/Au, RE= Ag/AgCl KCl 3 M, CE= Pt Mesh. Magnetization time: 120 seconds before the cyclic voltammetry.

8.2- Charge transport measurements through $NiAu^{TS}$/SAM//GaO_x/EGaIn junctions

Eutectic Gallium-Indium (EGaIn) was used as the top electrode in the fabricated junctions. For the charge transport studies presented in this work, SAMs were prepared on ultra-smooth template-stripped ($NiAu^{TS}$), whose ultra-flat topography promote low dispersion in the data.[6,7] We followed the standard procedure for the EGaIn tip generation.[10] All junctions were formed and measured with freshly prepared tips, exhibiting a geometrical contact area of around 300-800 µm2. The EGaIn electrode was biased while the $NiAu^{TS}$ substrate was grounded.

The electrical measurements with the "EGaIn technique" were performed with an in-house developed measurement setup (**Figure S19**). Most of the components were purchased from Thorlabs. The setup is mounted on an optical table to avoid vibrations. The top-electrode (EGaIn) was biased and the bottom electrode was grounded. The JV curves were acquired using a Keithley 2004B. The Keithley was controlled using the software developed in LabVIEW. Different junctions were prepared and several traces for each junction were registered in the form of JV curves. To obtain representative values, the data were treated statistically to determine the mean and the standard deviation. All the measurements were performed under ambient conditions: (T = 21 ± 2 ºC; RH = 45 ± 10 %). To perform spin-dependent charge transport measurements, we adapted our EGaIn set-up to incorporate the permanent magnet (H = 0.4 T) underneath the Ni/Au^{TS} substrate.

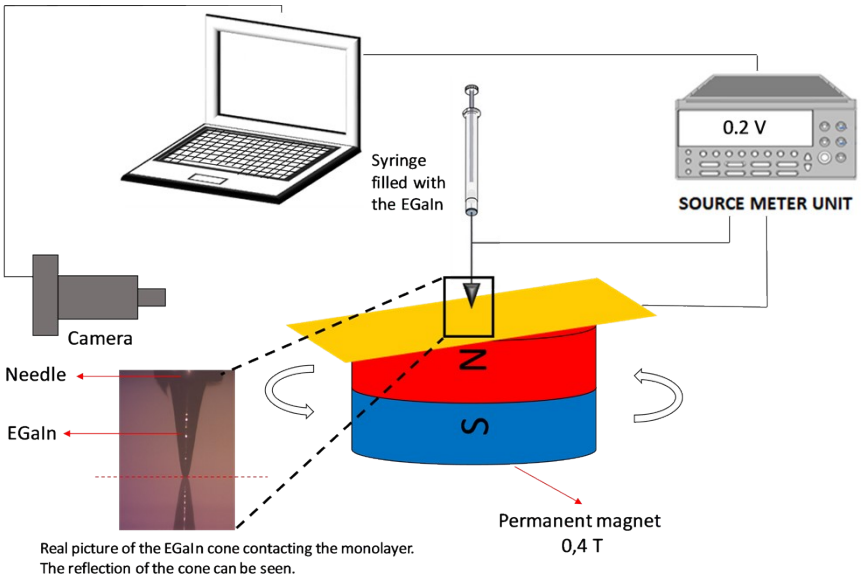

Figure S19. Scheme of the setup used for the electrical characterization system by performing spin-dependent current *versus* voltage measurements using the EGaIn tip as the top electrode.

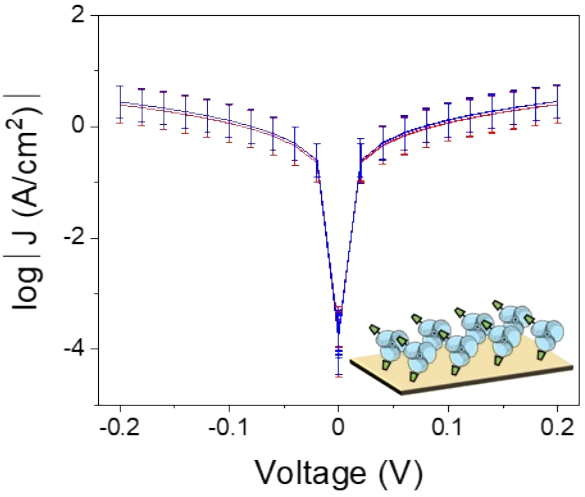

Figure S20. Semilog plot of current density (J) *vs.* Voltage (V) for NiAu^{TS}/***(M)*-bPTM-SAM**//GaO_x/EGaIn junction. Experiments with magnet "up" (red) and "down" (blue).

Table S5. Statistics of the electrical characterization of the enantioenriched SAMs using the EGaIn electrode.

Surface	Magnet	Number of Junctions	Number of curves per junction	Total number of curves successfully measured	Yield%
NiAu^{TS}/*(P)*-bPTM-SAM	"up"	12	10	100	83
	"down"	11	10	80	73
NiAu^{TS}/*(M)*-bPTM-SAM	"up"	11	10	110	100
	"down"	11	10	110	100

8. Electron Transport Calculations

The electron-transport calculations were based on density functional theory (DFT) and non- equilibrium Green's functions (NEGF). For this, we used the code ANT[11–15] which interfaces with Gaussian 09[16] and also includes an implementation of the spin-orbit coupling (SOC) [17] based on optimized gaussian basis sets.[18] The LANL2DZ[19] basis set was employed for all atoms except for the gold atoms in the outermost layers and the side surfaces, for which a CRENBS[20] basis set was used. PBE[21] was employed as exchange-correlation functional.

9. References

[1] F. Bejarano, I. J. Olavarria-Contreras, A. Droghetti, I. Rungger, A. Rudnev, D. Gutiérrez, M. Mas-Torrent, J. Veciana, H. S. J. Van Der Zant, C. Rovira, E. Burzurí, N. Crivillers, *J. Am. Chem. Soc.* **2018**, *140*, 1691.

[2] V. Diez-Cabanes, G. Seber, C. Franco, F. Bejarano, N. Crivillers, M. Mas-Torrent, J. Veciana, C. Rovira, J. Cornil, *ChemPhysChem* **2018**, *19*, 2572.

[3] P. Ravat, *Chem. Eur. J.* **2021**, *27*, 3957.

[4] M. Rickhaus, L. Jundt, M. Mayor, *Chimia* **2016**, *70*, 192.

[5] P. C. Mondal, C. Fontanesi, D. H. Waldeck, R. Naaman, *ACS Nano* **2015**, *9*, 3377.

[6] N. Vogel, J. Zieleniecki, I. Köper, *Nanoscale* **2012**, *4*, 3820.

[7] A. Alessandrini, C. A. Bortolotti, G. Bertoni, A. Vezzoli, P. Facci, *J. Phys. Chem. C* **2008**, *112*, 3747–3750.

[8] A. J. Bard, L. R. Faulkner, *Electrochemical Methods; Fundamentals and Applications*, John Wiley & Sons, Ltd, **2002**.

[9] A. L. Eckermann, D. J. Feld, J. A. Shaw, T. J. Meade, *Coord. Chem. Rev.* **2010**, *254*, 1769.

[10] X. Chen, H. Hu, J. Trasobares, C. A. Nijhuis, *ACS Appl. Mater. Interfaces* **2019**, *11*, 21018.

[11] J. J. Palacios, A. J. Pérez-Jiménez, E. Louis, E. SanFabián, J. A. Vergés, *Phys. Rev. B* **2002**, *66*, 035322.

[12] J. J. Palacios, A. J. Pérez-Jiménez, E. Louis, J. A. Vergés, *Phys. Rev. B.* **2001**, *64*, 115411.

[13] D. Jacob, J. J. Palacios, *J. Chem. Phys.* **2011**, *134*, 044118.

[14] https://www.simuneatomistics.com/

[15] https://github.com/juanjosepalacios/ANT.Gaussian

[16] M. J. Frisch et al., Computer code GAUSSIAN09, Revision C.01, Gaussian, Inc. Wallingford, CT, **2009**

[17] S. Pakdel, M. Pourfath, J. J. Palacios, *Beilstein J. Nanotechnol.* **2018**, *9*, 1015.

[18] W. Dednam, L. A. Zotti, S. Pakdel, E. Lombardi, J. Palacios, *Proc. 65th Annual Conf. South African Institute of Physics*, **2022**, 65, 25.

[19] W. R. Wadt, P. J. Hay, *J. Chem. Phys.* **1985**, *82*, 284.

[20] R. B. Ross, J. M. Powers, T. Atashroo, W. C. Ermler, L. A. LaJohn, P. A. Christiansen, *J. Chem. Phys.* **1990**, *93*, 6654.

[21] J. P. Perdew, K. Burke, M. Ernzerhof, *Phys. Rev. Lett.* **1996**, *77*, 3865.